Supporting Information

Engineering the Amorphous-to-Crystalline Transformation, Fluorescence Enhancement and Reversible Switching of a Cyclobutane Derivative inside a Polymer Film

Supriya Kar[a], Sonu Kumari[b], Ram Singh Jat[b], Ch. Suresh[a], S. Rajagopala Reddy[b], M. Bhanuchandra[c] and Chanchayya Gupta Chandaluri*[a]

[a.] *Supriya Kar, Ch. Suresh and Dr. Ch Gupta Chandaluri, Department of Humanities and Sciences, Chemistry Division, Indian Institute of Petroleum and Energy, Visakhapatnam, Andhra Pradesh-530003, India.*

[b.] *Sonu Kumari, Ram Singh Jat, and Dr. S. Rajagopala Reddy, Department of Chemistry, Central University of Rajasthan, Bandarsindri, Rajasthan-305817, India.*

[c.] *Dr. M. Bhanuchandra, Department of Chemistry, University of Delhi, Delhi-110007, India.*

Table of Contents

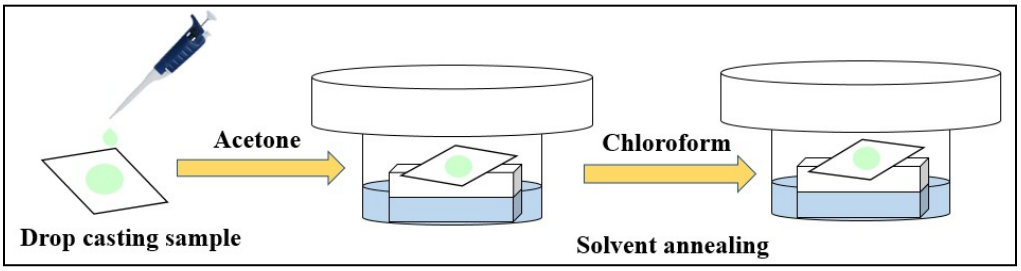

Figure S1: Schematic diagram of *vapochromic* process

1. Single Crystal X-ray Structure of CB:

Table S1: Crystal data and structure refinement for CB.

Empirical formula	$C_{36}H_{28}N_4$
Formula weight	516.62
Temperature	293(2)
Crystal system, space group	Monoclinic, C2/c
Unit cell dimensions	a = 21.151(4) Å α = 90°
	b = 11.6110(18) Å β = 105.710(18)°
	c = 11.946(2) Å γ = 90°
Volume	2824.0(8) $Å^3$
Z	4
ρcalc. / g cm^{-3}	1.215
μ / mm^{-1}	0.072
Temperature/K	293
2Θ range for data collection/°	5.718 to 52.744
Reflections collected	5608
Independent reflections	2882 [R_{int} = 0.0864, R_{sigma} = 0.1947]
Data/restraints/parameters	2882/0/182
Goodness-of-fit	0.868
Final R indexes [I>=2σ (I)]	R_1 = 0.0625, wR_2 = 0.0709
Largest diff. peak and hole / e$Å^{-3}$	0.14/-0.18

(a)

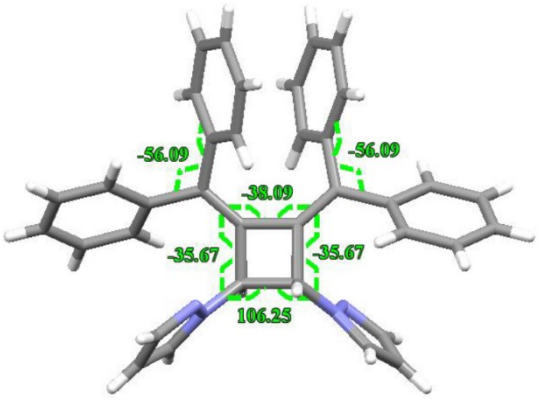
-56.09
-56.09
-38.09
-35.67
-35.67
106.25

(b)

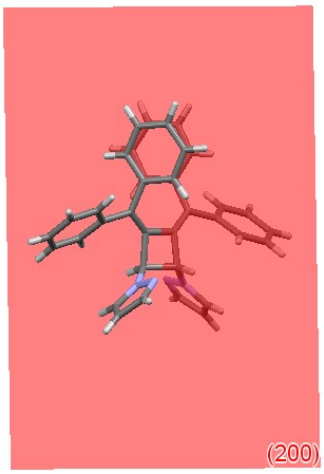
(200)

(c)

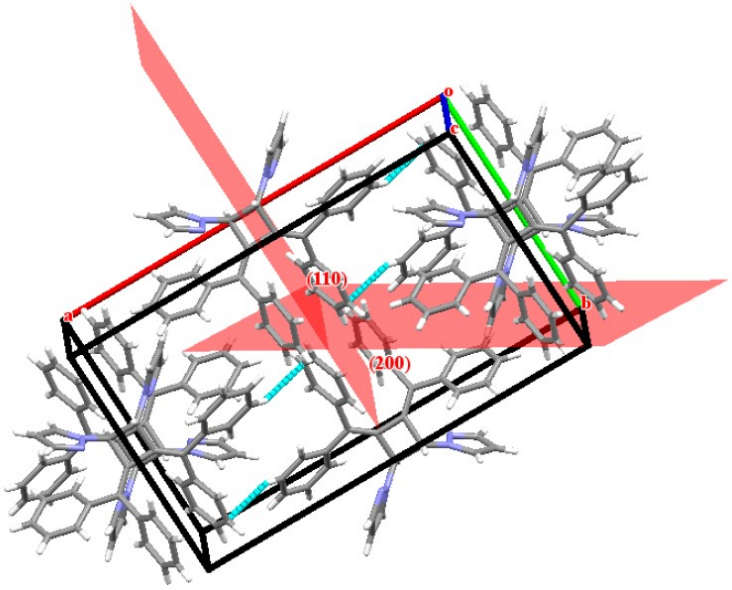
o
c
a
b
(110)
(200)

(d)

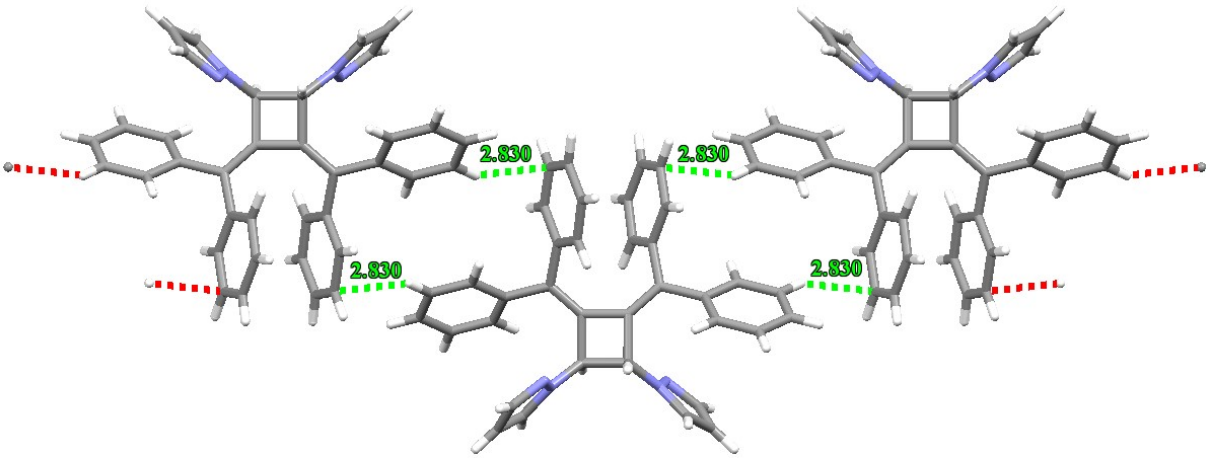
2.830
2.830
2.830
2.830

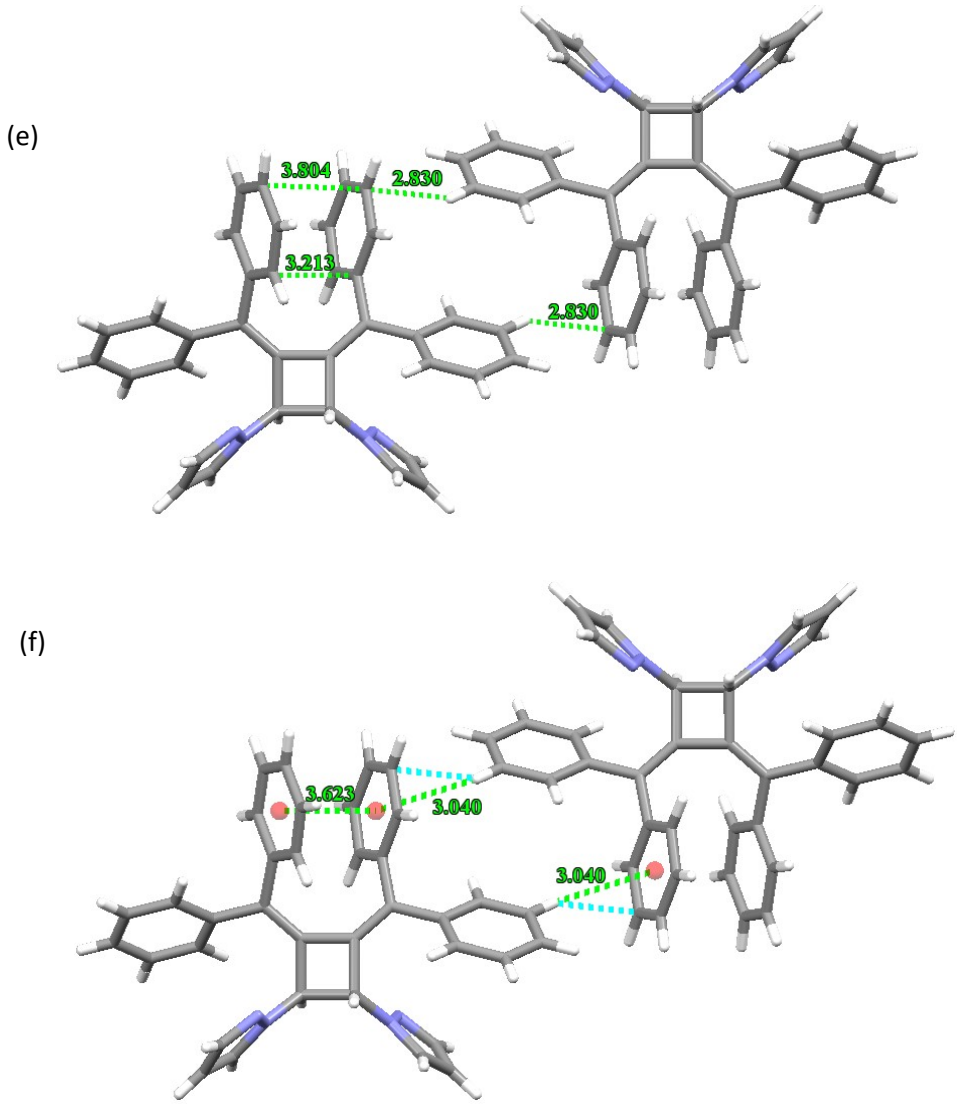

Figure S2: (a) Torsion angles of CB (b) plane (200) intersecting the monomer from the center (c) molecular packing along with planes (d) C-H-Π (cyan broken line) short intermolecular contacts leading to layer structures (e) intramolecular distances between the benzene rings (f) Π-Π and C-H-Π intermolecular distance between neighboring molecule. C (black) and N (blue) atoms are indicated.

2. Spectroscopic and microscopic analysis for colloids

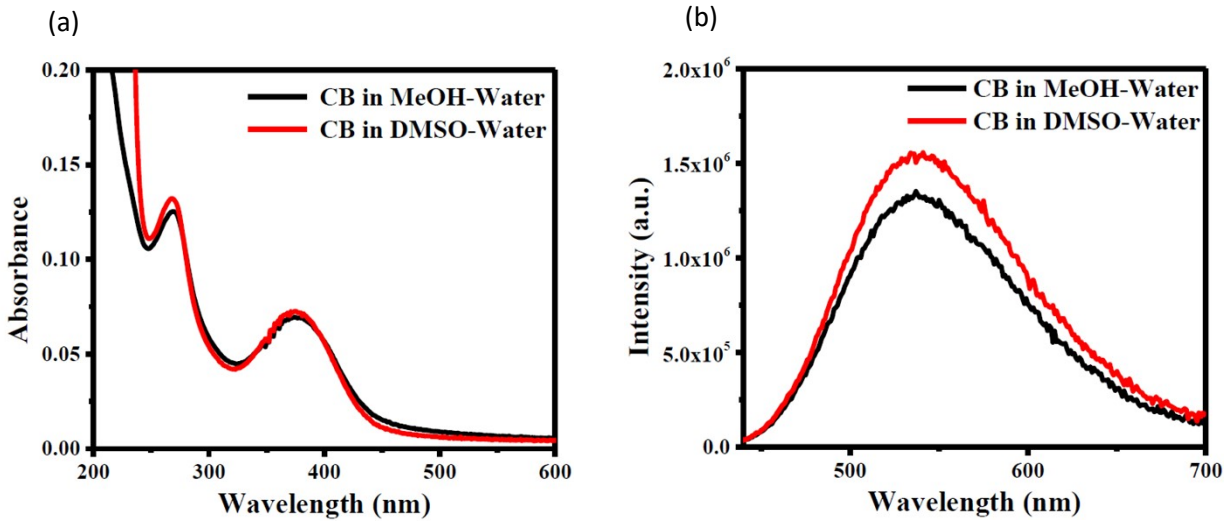

Figure S3: (a) Electronic absorption spectra and (b) fluorescence emission spectra of CB colloids prepared in Methanol-Water and DMSO-Water system.

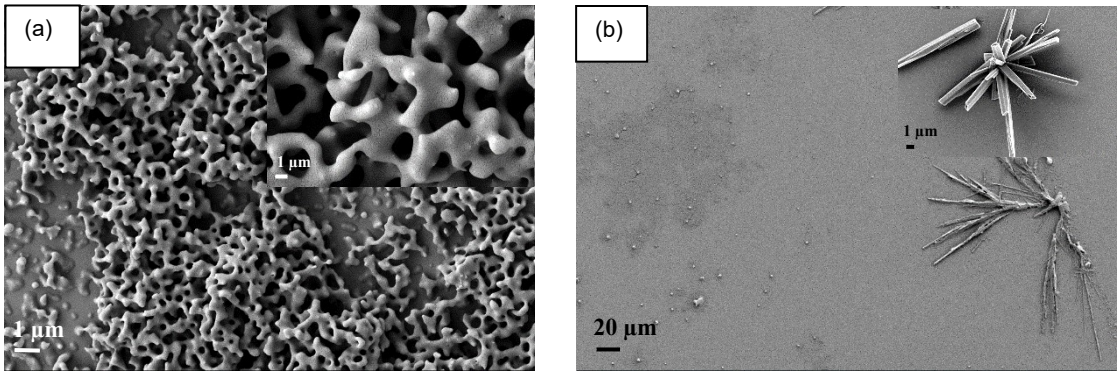

Figure S4: SEM images of (a) CB- CH_3OH colloid (b) CB-DMSO colloid

3. Procedure for Quantum yield calculation

Quantum yield of solution was measured using Coumarin 102 as a reference (ϕ_f = 73%, λ_{ex} = 373 nm, Ethanol) and for colloid was measured using Quinine sulphate (ϕ_f = 54.6%, λ_{ex} = 350 nm, 1N H_2SO_4). For this, sample solution and reference solution were prepared with nearly similar absorbance. The sample was placed on a solid sample holder at the right angle geometry for the recording of spectra. The following equation used for the calculation of quantum yield;

$$\Phi f = \Phi f,s \times \frac{F_X}{F_s} \times \frac{f_s}{f_x} \times \frac{n_X^2}{n_S^2} \quad \text{..... (Eqn. 1)}$$

$$f = 1 - 10^{-A_{\lambda ex}} \quad \text{..... (Eqn. 2)}$$

Where, n, F, and Φ are the refractive index, integral fluorescence, and fluorescence quantum yield, respectively, where the subscripts s and x refer to the standard and sample respectively. λ_{ex}, ε, and A, denote the excitation wavelength, molar extinction coefficient (L mol^{-1} cm^{-1}), and absorbance, respectively.

S.No.	Sample	Absorption max (nm)	Emission max (nm)	Q.Y(%)
1	CB in CH_3OH solution	367	591	0.15
2	CB in CH_3OH –water colloid	375	538	4.5
3	Solid CB	~400 (broad)	510	70

Table S2: Absorption max (λ_{max}), emission max (λ_{emmax}) and quantum yield for CB in CH_3OH solution, CB in CH_3OH-water colloid and solid CB

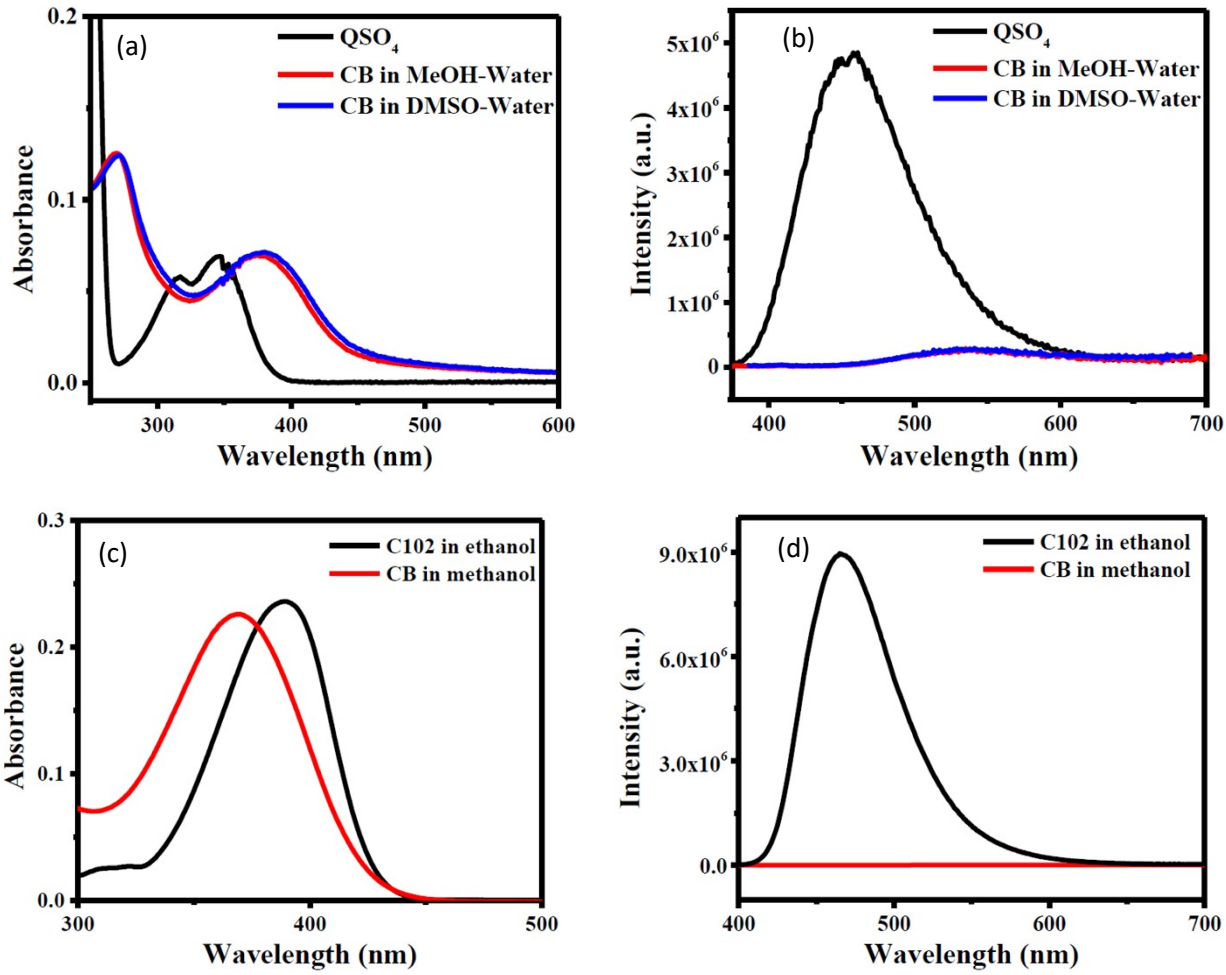

Figure S5: (a) Absorption and (b) emission spectra of CB in methanol and CB in DMSO measured using quinine sulphate as a reference (c) absorption and (d) emission spectra of CB in methanol measured using coumarin 102 as a reference

4. Microscopic analysis, Quantum yield values and images under UV 365nm lamp of drop casted films

Drop casted CB-THF solution onto a glass slide results in the formation of a layer on the substrate. SEM analysis reveals the cracks in the film formed at room temperature (Figure S6) and domains are observed in the film fabricated at 100°C (Figure S7). The film fabricated under vacuum exhibits uniform morphology as shown in the Figure S8. Films prepared using THF as solvent does not have any nano/micro particles.

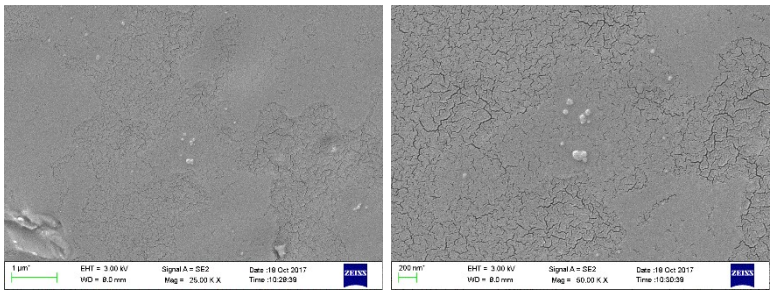

Figure S6: SEM images of films obtained by drop casting CB-THF solution followed by air dry.

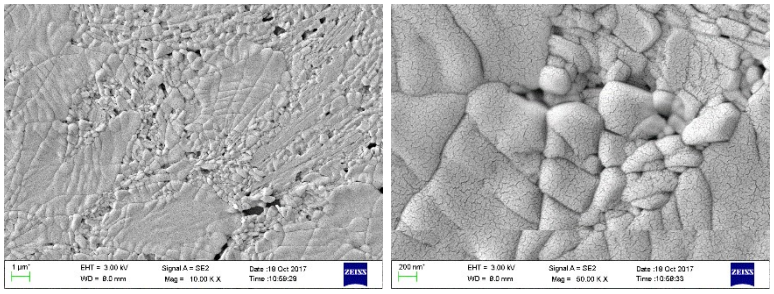

Figure S7: SEM images of films obtained by drop casting CB-THF solution followed by drying at 100°C

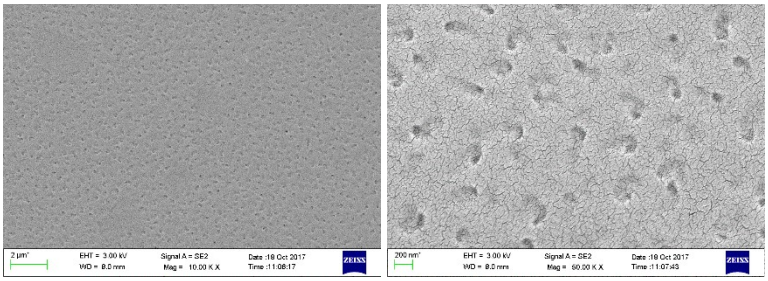

Figure S8: SEM images of films obtained by drop casting CB-THF solution followed by drying under vacuum

Drop casted CB-methanol solution onto a glass slide results in the formation of a spherical particles at room temperature (Figure S9) and connected particles were observed in the film fabricated at 100ºC (Figure S10). The film fabricated under vacuum exhibits morphology of networking large number of particles as shown in the Figure S11.

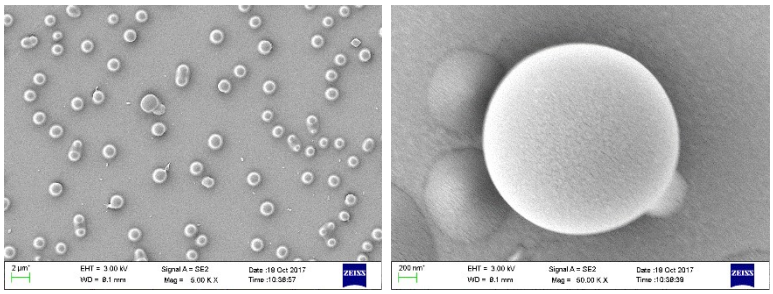

Figure S9: SEM images of films obtained by drop casting CB-methanol solution followed by air dry.

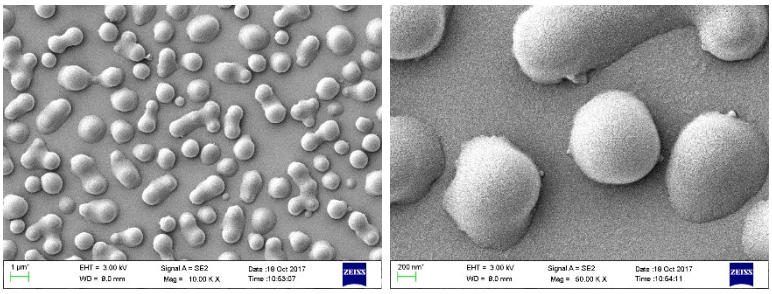

Figure S10: SEM images of films obtained by drop casting CB-methanol solution followed by air dry at 100ºC.

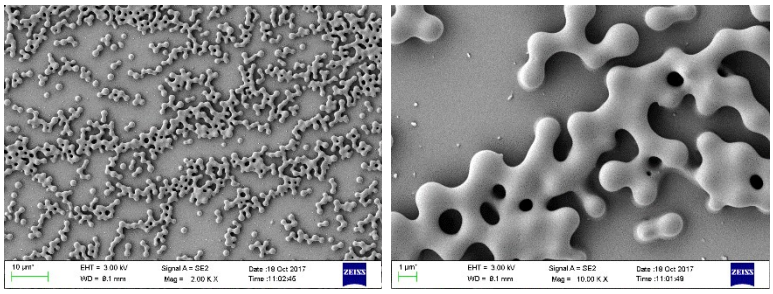

Figure S11: SEM images of films obtained by drop casting CB-methanol solution followed by vacuum.

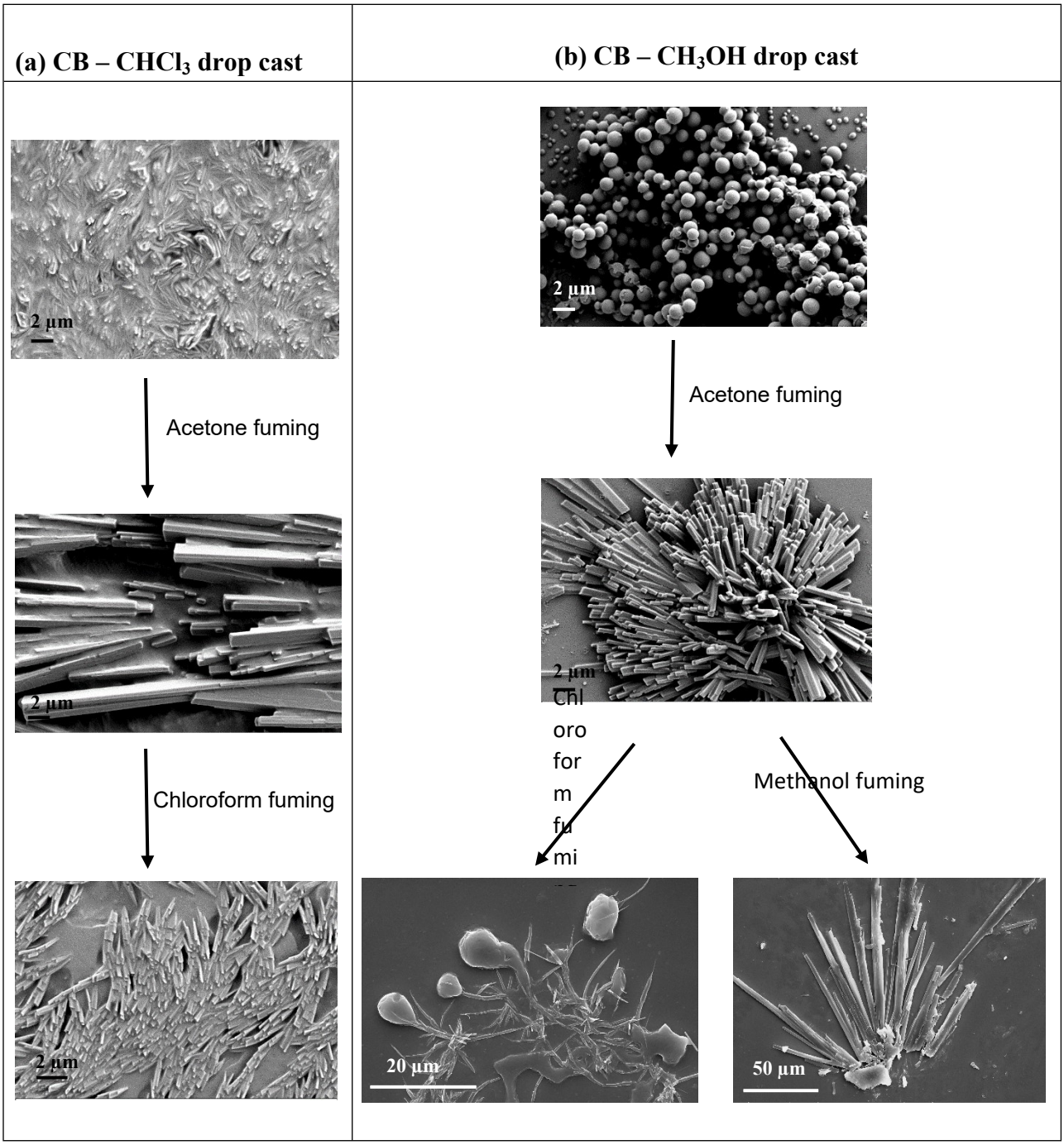
(a) CB – CHCl3 drop cast
(b) CB – CH3OH drop cast
2 µm
Acetone fuming
2 µm
Chloroform fuming
2 µm
2 µm
Acetone fuming
2 µm
Chloroform fuming
Methanol fuming
20 µm
50 µm

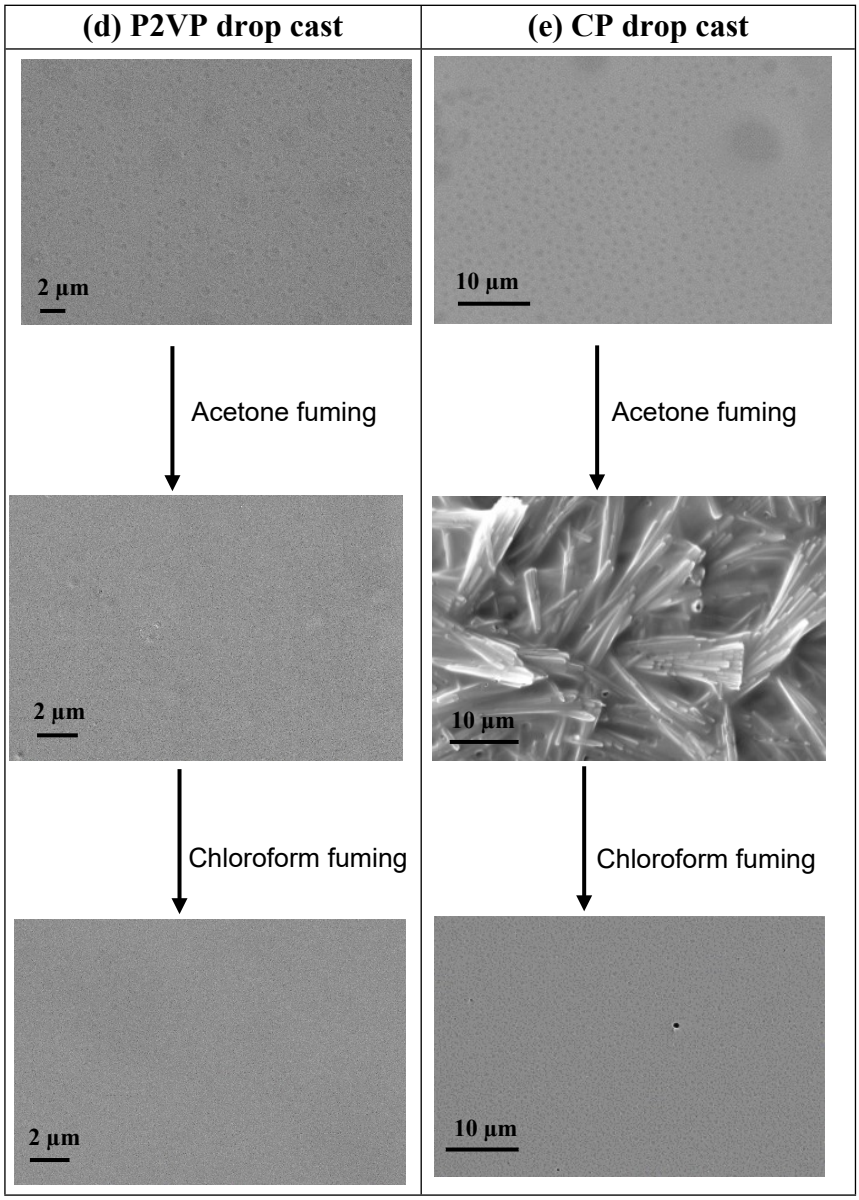

Figure S12: SEM images of drop cast before and after fuming of CB-chloroform, CB-CH_3OH,

S. No.	Sample	λ_{max} (nm)	$\lambda_{em\ max}$ (nm)	Q. Y. (%)

P2VP and CP

Table S3: Absorption max, emission max and quantum yield for CP, CPA and CPAC

1	CP	410 (broad)	528	12
2	CPA	370 (broad)	504	19
3	CPAC	410 (broad)	528	14

Four thin films were fabricated using drop-casting CB methanol solution onto a glass substrate. These films were subsequently exposed to acetone vapors followed by either chloroform (Table S4) or methanol (Table S5) vapors. In both cases, the crystalline to amorphous conversion was incomplete, as the films exhibited strong fluorescence under UV 365nm lamp compared to the initial amorphous films.

	1	**2**	**3**	**4**
CB-CH_3OH drop cast **(Amorphous)**		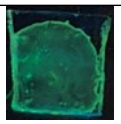		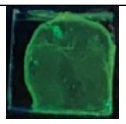
Acetone fuming **(Crystalline)**		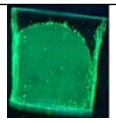		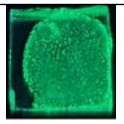
Chloroform fuming **(both amorphous and crystalline)**	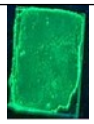	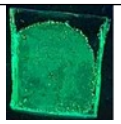		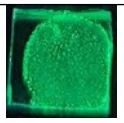

Table S4: Images of thin films of CB-CH_3OH and after solvent (acetone followed by chloroform) fuming under 365 nm lamp

Table S5: Images of thin films of CB-CH_3OH and after solvent (acetone followed by methanol) fuming under 365 nm lamp

	1	2	3	4
CB-CH_3OH drop cast **(Amorphous)**	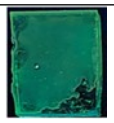	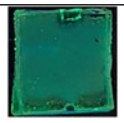	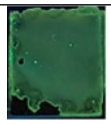	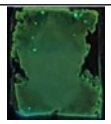
Acetone fuming **(Crystalline)**	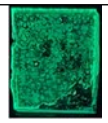	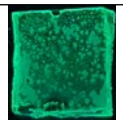	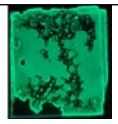	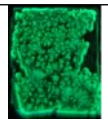
Methanol fuming **(both amorphous and crystalline)**	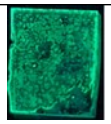	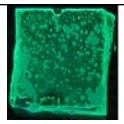	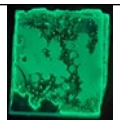	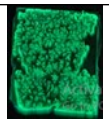

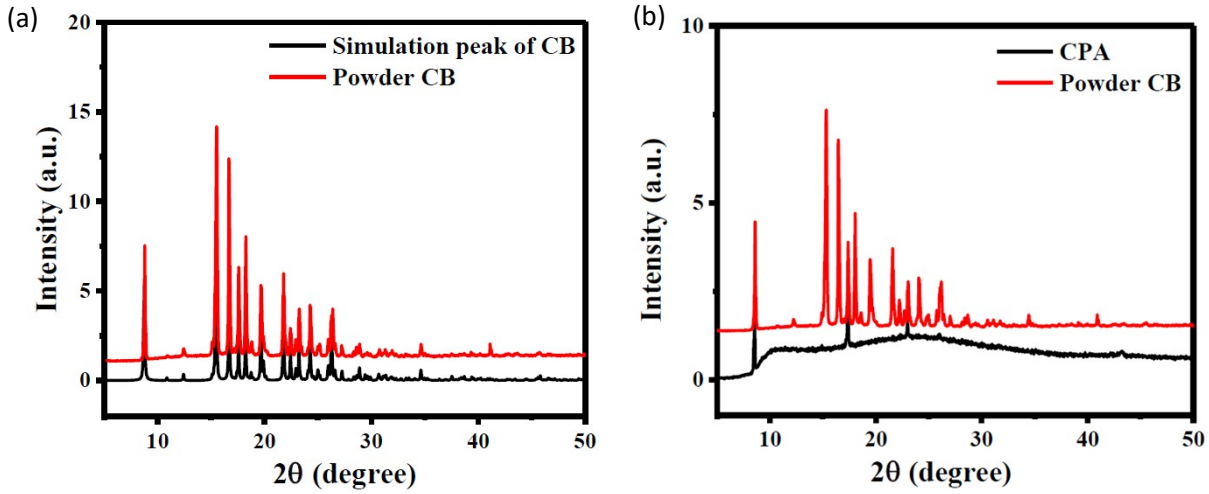

5. Simulated x-ray and powder x-ray diffraction pattern

The x-ray diffraction pattern of the CB powder sample was recorded using Bruker D8 Advance A25 X-ray diffractometer with Cu Kα radiation (λ = 1.54060 A˚) at 40 kV and 40 mA. The patterns were simulated based on the single crystal structure determined at room temperature, as shown below.

Figure S13: XRD pattern of (c) ital XRD data and the powdered CB (b) powdered C c) diffraction peaks of CPA film with Miller indices.

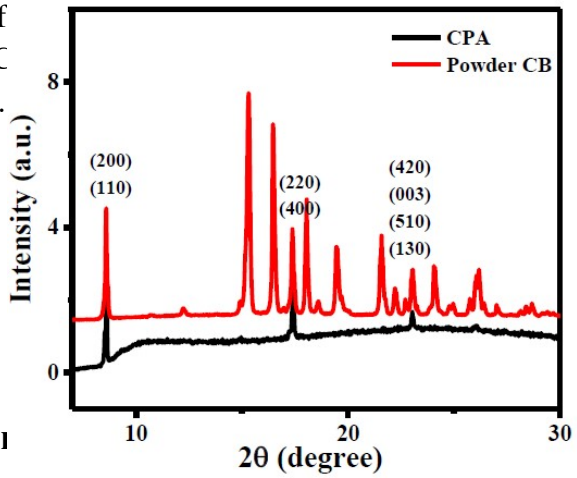

6. Confocal laser scanni

Table S6: Scanning electron microscope (SEM) images, confocal laser scanning microscope images (CLSM), average lifetime images, histogram of CP drop cast film, film after fuming, CB in chloroform drop cast, CB in methanol drop cast and solid CB

S.No.	Sample description	SEM image	CLSM image	Avg lifetime image	Histogram
1	CP	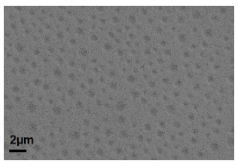	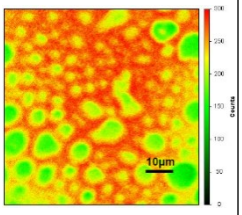	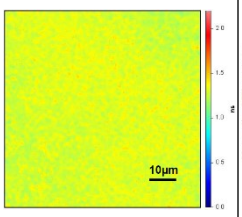	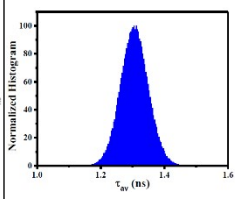

6	**Solid CB**	**----**	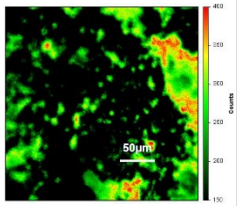	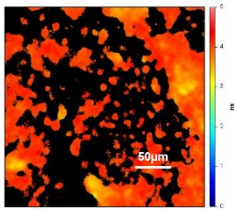	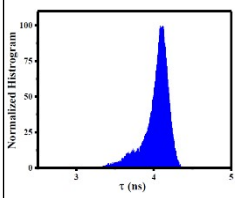
2	**CPA**	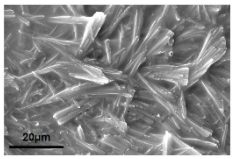	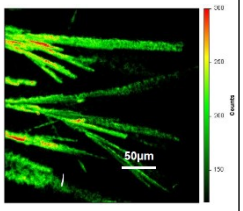	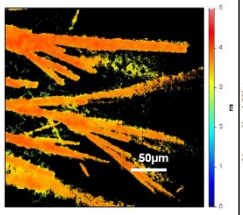	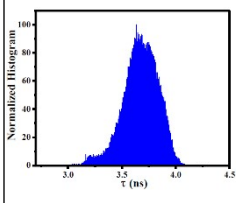
3	**CPAC**	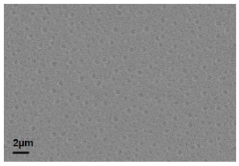	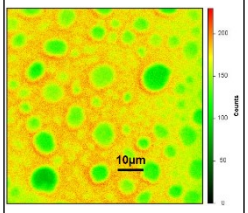	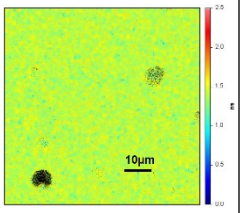	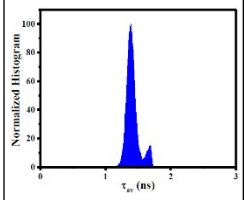
4	**CB in $CHCl_3$ drop cast**	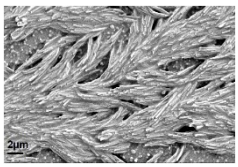	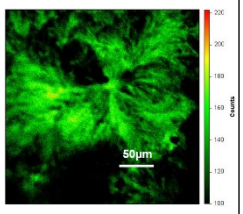	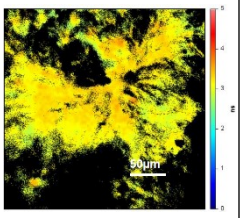	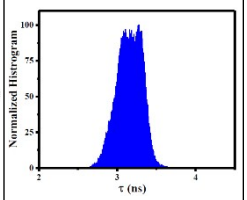
5	**CB in CH_3OH drop cast**	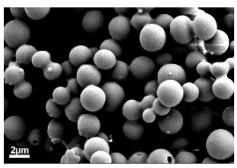	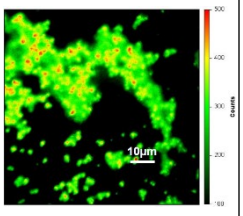	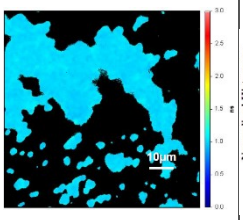	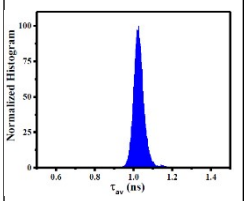

Table S7: Details of the excited state lifetime of CP drop cast film, film after fuming, CB in chloroform, methanol drop cast and solid CB. (Data obtained from a single point in the film and the

data fitted with single or multiple exponential decays based on the χ^2 value using VistaVision software)

Sample	τ_1 (ns)	α_1	τ_2 (ns)	α_2	τ_{aw} (ns)	τ_{iw} (ns)	χ^2
CP	0.98	0.75	2.44	0.25	1.4	1.6	1.0
CPA	3.85	1.0	–	–	3.9	3.9	1.01
CPAC	0.94	0.69	2.35	0.31	1.4	1.7	1.10
CB in $CHCl_3$ drop cast	3.45	1.0	–	–	3.5	3.5	1.10
CB in methanol drop cast	0.84	0.85	2.16	0.15	1.0	1.3	1.0
CB solid powder	4.17	1.0	–	–	4.2	4.2	1.08

The average lifetime (τ) is calculated using the following expressions:

$$\tau aw = \alpha 1\tau 1 + \alpha 2\tau 2$$

$$\tau iw = \frac{\alpha 1\tau_1^2 + \alpha 2\tau_2^2}{\alpha 1\tau 1 + \alpha 2\tau 2}$$

Where τaw is Amplitude-Weighted Lifetime and τiw is Intensity-Weighted Lifetime, α_1 and α_2 are pre-exponential factors, τ_1 and τ_2 are lifetime components.

Table S8: Details of the excited state average lifetime of the images obtained from CP drop cast film, film after fuming, CB in chloroform, methanol drop cast and solid CB. (Data collected from the total image)

Sample	τ_1 (ns)	α_1	τ_2 (ns)	α_2	τ_{av} (ns)
CP	0.7- 1.2	0.6 – 0.85	1.8 – 2.8	0.25 – 0.4	1.2 – 1.4
CPA	3.4 – 4.0	1.0	–	–	3.4 – 4.0
CPAC	0.6 – 1.4	0.55 – 0.90	1.8 – 2.8	0.10 – 0.45	1.3 – 1.65
CB in $CHCl_3$ drop cast	2.8 – 3.5	1.0	–	–	2.8 – 3.5
CB in methanol drop cast	0.6 – 1.0	0.80 – 0.95	1.7 – 2.4	0.05 – 0.20	0.95 – 1.15
CB solid powder	3.7 - 4.30	1.0	–	–	3.7 - 4.30

7. Amorphous to crystalline transformation using other polymers

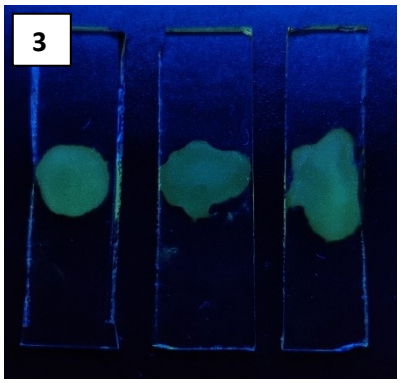

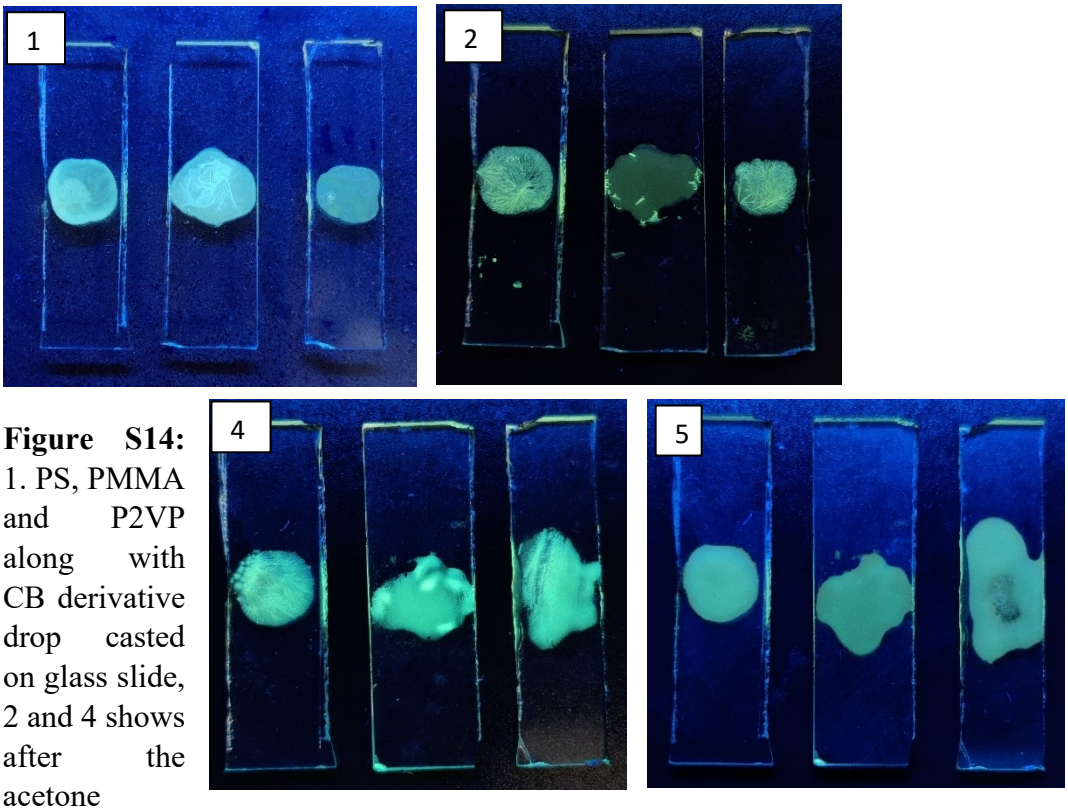

Figure S14: 1. PS, PMMA and P2VP along with CB derivative drop casted on glass slide, 2 and 4 shows after the acetone annealing, 3 and 5 shows after chloroform annealing

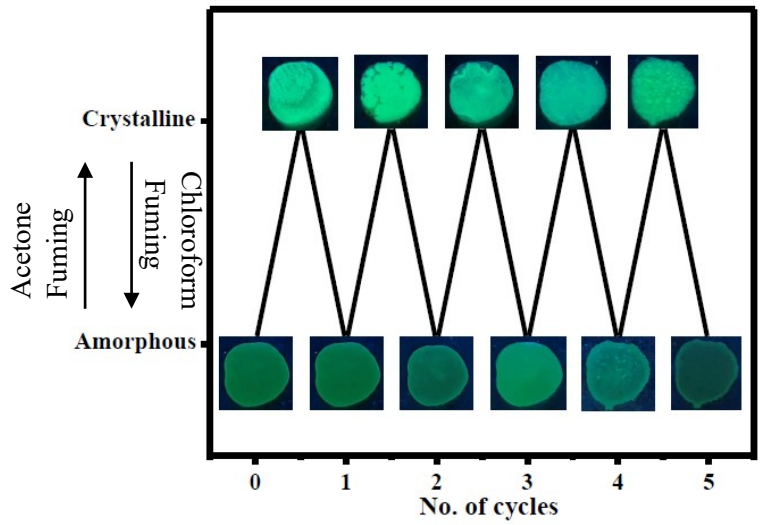

Figure S15: Images of thin films of CP (amorphous to crystalline transformations) under 365 nm lamp for five cycles

8. Chromaticity diagram

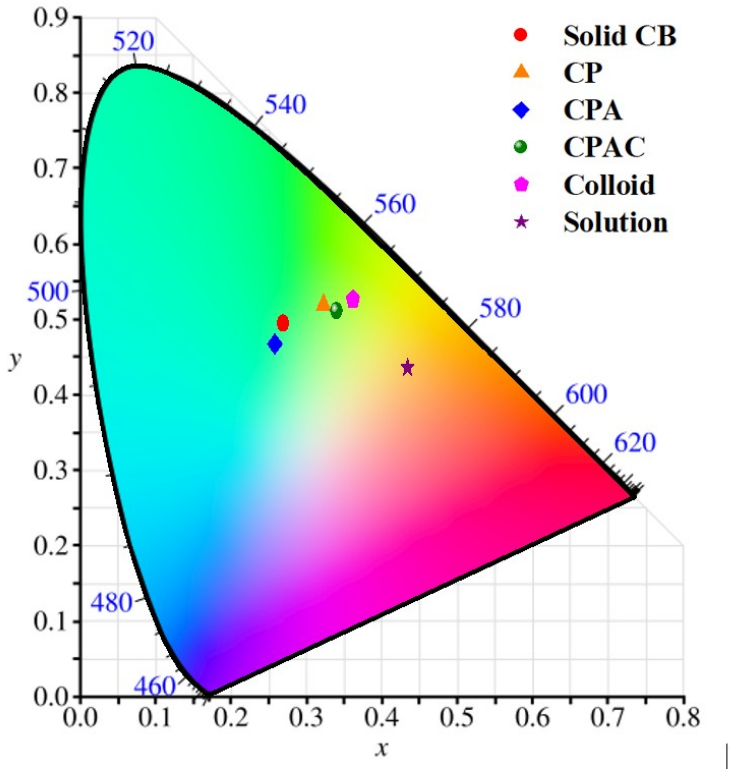

Figure S16: Chromaticity diagram of solid CB, CP thin film and after solvent fuming, CB-methanol/water colloid and CB in methanol solution.

9. Computational Data

To understand the steady state spectroscopy, we performed computational chemistry calculations. The ground state geometry of CB is optimized using density functional B3LYP1-5[1–5] and the basis set 6-31g(d,p).[6–9] The geometry is stable on the account of all positive frequencies. Solvent effects are incorporated by using the CPCM model.[10–16] The vertical excited states are calculated at TD-DFT level. To understand the Stoke shift, we have performed the optimization of the S_1 state. To mimic the solid state environment, we have taken the geometry of CB from the crystal structure and used it without performing geometry optimization. All the calculations are performed using the ORCA electronic structure program package.[17–20] Natural transition orbital analysis based on TD-DFT one-particle density matrix is performed to characterize the excited states as local excitation (LE) and charge transfer states (CT) using Theodore program package.[21] For this purpose, CB was fragmented into diphenyl methylene, cyclobutane and pyrazole. Based on the natural transition orbitals, excitations of S_1, S_2 and S_3 are decomposed to local excitation in diphenyl methylene (LDP), local excitation in cyclobutane (LCB), local excitation in pyrazole (LP) and charge transfer excitations between these fragments. CT1 is the charge transfer between the fragments cyclobutane to diphenyl methylene. CT2 is the charge transfer state between diphenyl methylene to pyrazole. CT3 is the charge transfer state between cyclobutane to pyrazole.

Table S9 presents the first 5 excited states of CB in methanol solvent, vacuum and solid environment. The wavelength (nm), oscillator strength (dimensionless) and the type of electronic excitation are provided. The S_1 state is located at 387 nm and is a bright state (bright states are the electronic states with considerable oscillator strength). The excitation energy is under estimated by the TD-DFT by ~30 nm. The adiabatic excitation energy obtained by optimizing the S_1 state by TD-DFT is 578 nm, resulting in a Stoke shift of ~191 nm compared to the experimental value of ~226 nm.

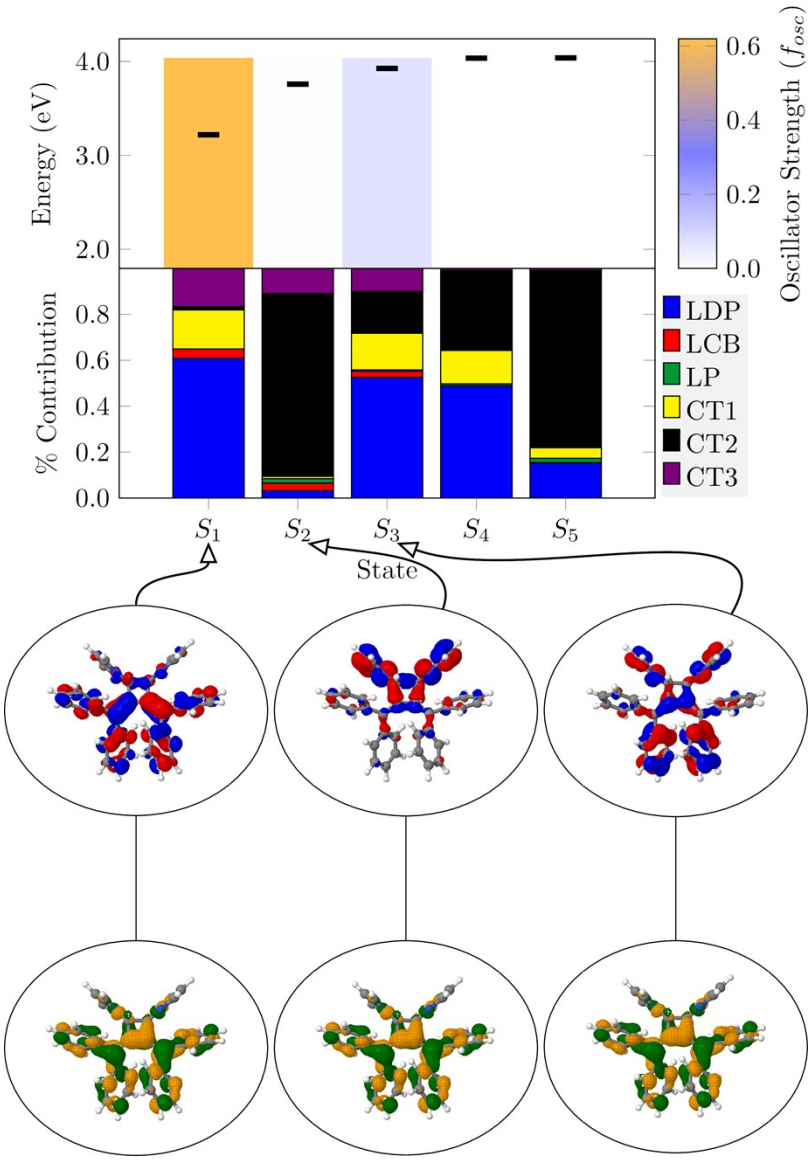

Figure S17: Fragment based analysis of excited states (S_1–S_5) of CB from TD-DFT/B3LYP/6-31G(D,P) calculation using Theodore program package. The first five excited states for the CB decomposed into contributions from local excitations (L) of ligands diphenylmethylene (LDP), cyclobutane (LCB), pyrazole (LP). Charge transfer (CT) states of cyclobutane to diphenylmethylene (CT1), diphenylmethylene to pyrazole (CT2), cyclobutane to pyrazole (CT3). Top: The excitation energies (thick horizontal bar, in eV) and oscillator strengths (in color) of the electronic states. Middle: Stacked bar chart showing the % contributions of LDP, LCB, LP, CT1, CT2 and CT3 excitations in the electronic states. Bottom: Representative Natural Transition Orbitals (NTOs) and dominant electronic transitions for states S_1, S_2 and S_3.

Table S9: The vertical excitation wavelength (λ in nm), oscillator strength (f in dimensionless), electron transitions and character of the state of CB in solution, vaccum and solid phases.

	State	λ (nm)	*f*	Electron transition	Character
Methanol	S_1	387	0.679	HOMO → LUMO	LE
	S_2	328	0.005	HOMO-1 → LUMO	CT
	S_3	314	0.051	HOMO-2 → LUMO	LE
	S_4	308	0.001	HOMO-4 → LUMO	CT
	S_5	306	0.002	HOMO-3 → LUMO	CT
Vaccum	S_1	385	0.619	HOMO → LUMO	LE
	S_2	330	0.003	HOMO-1 → LUMO	CT
	S_3	316	0.070	HOMO-2 → LUMO	LE
	S_4	307	<0.001	HOMO-4 → LUMO	CT
	S_5	307	0.005	HOMO-3 → LUMO	CT
Solid	S_1	354	0.745	HOMO → LUMO	LE
	S_2	302	0.009	HOMO-2 → LUMO	CT
	S_3	301	0.054	HOMO-1→ LUMO	LE
	S_4	296	0.002	HOMO-3 → LUMO	CT
	S_5	292	0.002	HOMO-4 → LUMO	CT

To understand the steady-state spectroscopy in the solid state, we first examined a monomer extracted from the crystal structure. The S_1 state (HOMO → LUMO) appears at 354 nm and is a bright state with an oscillator strength of 0.745 (see Table S9 and Figure S18). Subsequently, we calculated the energies of the first 30 excited states using a series of molecular aggregates dimers, trimers, tetramers, pentamers, and hexamers that constructed from the unit cell of the crystal structure (see Figure S19 and Figure 1b). A total of 15 unique dimers can be generated from the unit cell containing six molecules (see Figure S19b). Analysis of the low-lying excited states of these dimers shows that the character of these states can be adequately described using only the HOMO and LUMO of each monomer (see Table S10 and Figure S20).

When the electronic transition involves the HOMO and LUMO of the same monomer, the state is classified as a locally excited (LE) state. In contrast, if the transition occurs between the HOMO of one monomer and the LUMO of another, the state is identified as a charge-transfer (CT) state. The dimer model yields two LE and two CT states. Depending on the relative orientation and intermolecular distance between the monomers, the excitation energies vary from 354.8 to 379.7 nm. Notably, the oscillator strength of one of the S_1–S_4 states is approximately twice that of the monomer and the remaining states are dark (negligible oscillator strengths).

With increasing aggregate size, the energy of the first excited state, although dark, shows a progressive red shift, whereas the bright state remains near 354 nm. In the pentamer and hexamer models, two bright states are observed: one around ~360 nm with an oscillator strength of 0.2, and another near ~355 nm with a significantly higher oscillator strength of 3.5. For the hexamer, the first excited state appears at 385 nm (See Table S14). Further extension of the molecular assembly in three dimensions is expected to red-shift the first excited state toward ~400 nm. These calculations were performed without incorporating the dielectric constant of the solid state. This model explains the red shift of the electronic absorption in solid CB.

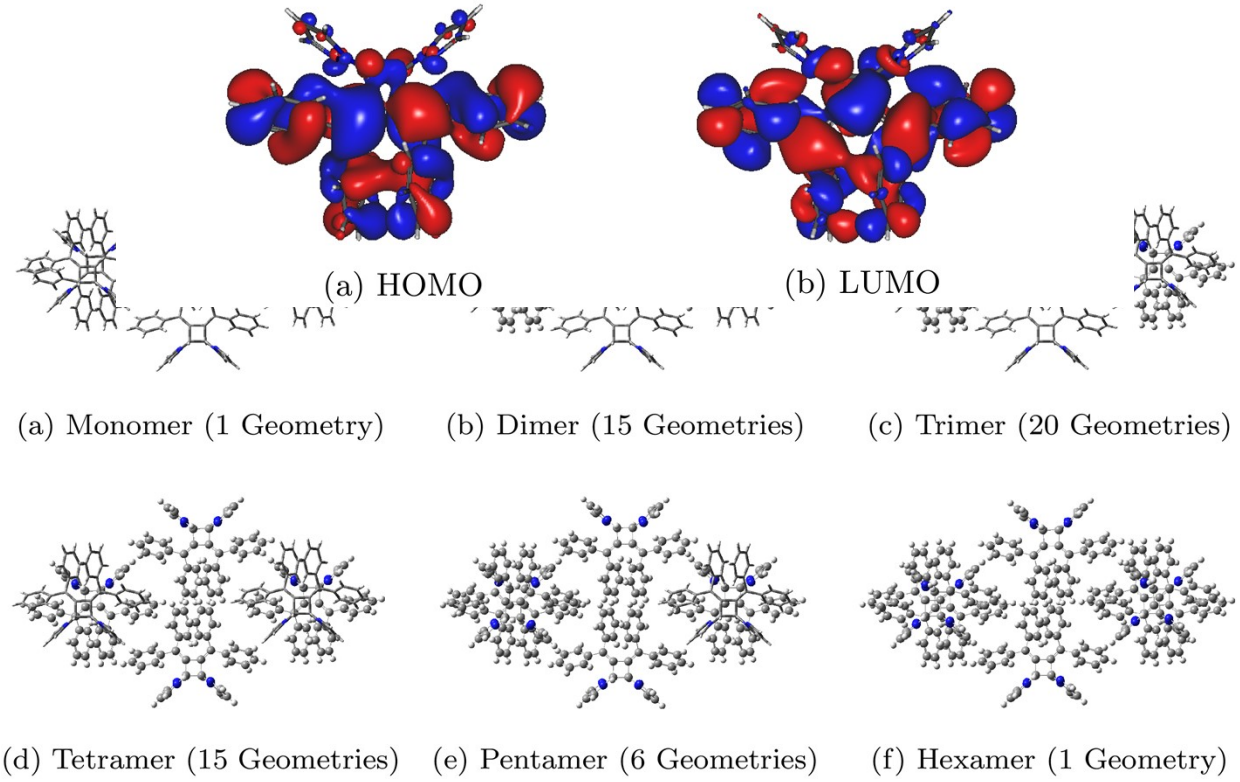

Figure S18: The molecular orbitals (a) HOMO and (b) LUMO of monomer extracted from crystal structure.

Figure S19: Description of the cluster model employed in the study. Six molecules were extracted from the crystallographic unit cell to construct the aggregates. In panels (a)–(f), two styles of molecular representation are used: a wire-frame model for the molecules that were discarded and a ball-and-stick model for the molecules included in the calculations. (a) Monomer; (b) one representative example from the fifteen possible dimers; (c) one representative example from the twenty possible trimers; (d) tetramer; (e) pentamer; and (f) hexamer.

Table S10: Vertical excitation wavelengths (λ, nm), oscillator strengths (f), electronic transitions, and corresponding characters for the selected dimer extracted from the unit cell.

State	λ (nm)	*f*	Electron transition	Character
S_1	355.5	1.54	HOMO → LUMO HOMO-1 → LUMO+1	LE
S_2	353.6	>0.01	HOMO → LUMO HOMO-1 → LUMO+1	LE
S_3	351.6	>0.01	HOMO-1→ LUMO	CT
S_4	351.6	>0.01	HOMO → LUMO+1	CT

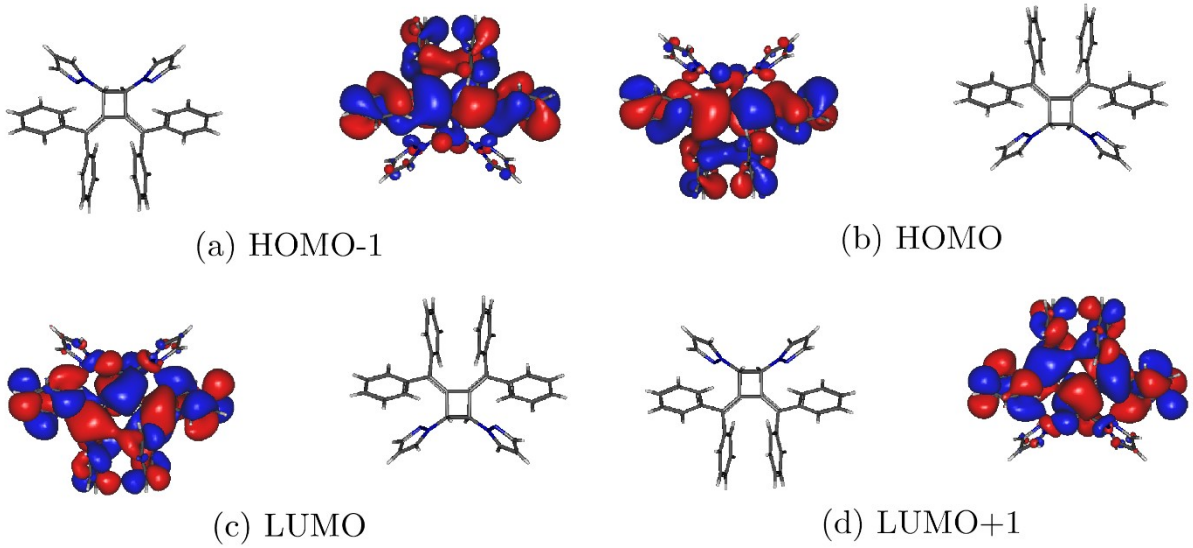

Figure S20: Frontier molecular orbitals from HOMO−1 to LUMO+1 of a representative dimer selected from the fifteen possible dimers extracted from the crystal structure.

Table S11: Vertical excitation wavelengths (λ, nm), oscillator strengths (f), electronic transitions, and corresponding characters for the selected trimer extracted from the unit cell.

State	λ (nm)	*f*	Electron transition	Character
S_1	378.1	>0.01	HOMO → LUMO	CT
S_2	378.1	>0.01	HOMO-1 → LUMO	CT
S_3	358.2	2.38	HOMO-2→ LUMO HOMO-1 → LUMO+1 HOMO → LUMO+2	LE

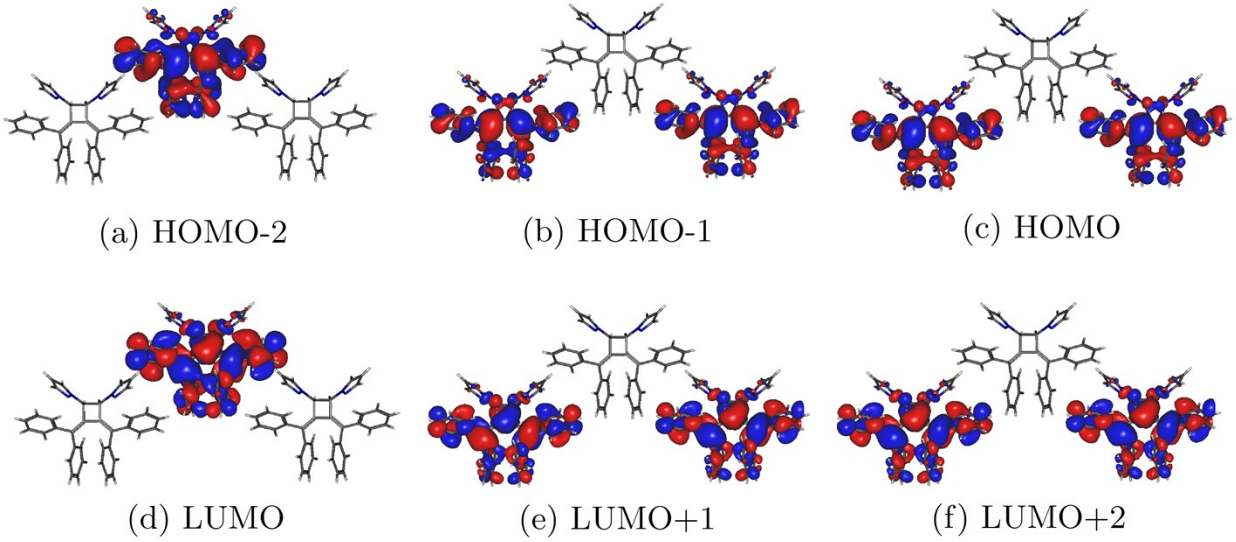

(a) HOMO-2 (b) HOMO-1 (c) HOMO

(d) LUMO (e) LUMO+1 (f) LUMO+2

S_4	354.3	>0.01	HOMO-1 → LUMO+2 HOMO → LUMO+1	LE
S_5	353.7	0.07	HOMO-2→ LUMO HOMO-1 → LUMO+1	LE
S_6	351.2	>0.01	HOMO → LUMO+2 HOMO-1 → LUMO+2 HOMO → LUMO+1	LE
S_7	351.2	>0.01	HOMO-1 → LUMO+1 HOMO → LUMO+2	LE
S_8	348.7	>0.01	HOMO-2 → LUMO+1	CT
S_9	348.7	>0.01	HOMO-2 → LUMO+2	CT

Figure S21: Frontier molecular orbitals from HOMO−2 to LUMO+2 of a representative trimer selected from the twenty possible trimers extracted from the crystal structure.

Table S12: The vertical excitation wavelength (λ, in nm units), oscillator strength (f, dimensionless), electron transition and character of the selected tetramer from the unit cell.

State	λ (nm)	*f*	Electron transition	Character
S_1	380.8	>0.01	HOMO → LUMO	CT
S_2	379.1	>0.01	HOMO-1 → LUMO	CT
S_3	377.1	>0.01	HOMO-2→ LUMO	CT
S_4	367.5	>0.01	HOMO → LUMO+1	CT
S_5	362	>0.01	HOMO-2→ LUMO+3	CT
S_6	359.5	>0.01	HOMO-1 → LUMO+1	CT
S_7	359.3	1.52	HOMO-2 → LUMO+1 HOMO → LUMO+3	LE
S_8	358.3	1.5	HOMO-3 → LUMO HOMO-1 → LUMO+2	LE
S_9	356.8	>0.01	HOMO-2 → LUMO+2	CT
S_{10}	354.2	0.08	HOMO-1 → LUMO+2	LE
S_{11}	352.5	>0.01	HOMO → LUMO+2	CT
S_{12}	351	0.11	HOMO-2 → LUMO+1 HOMO → LUMO+4	LE

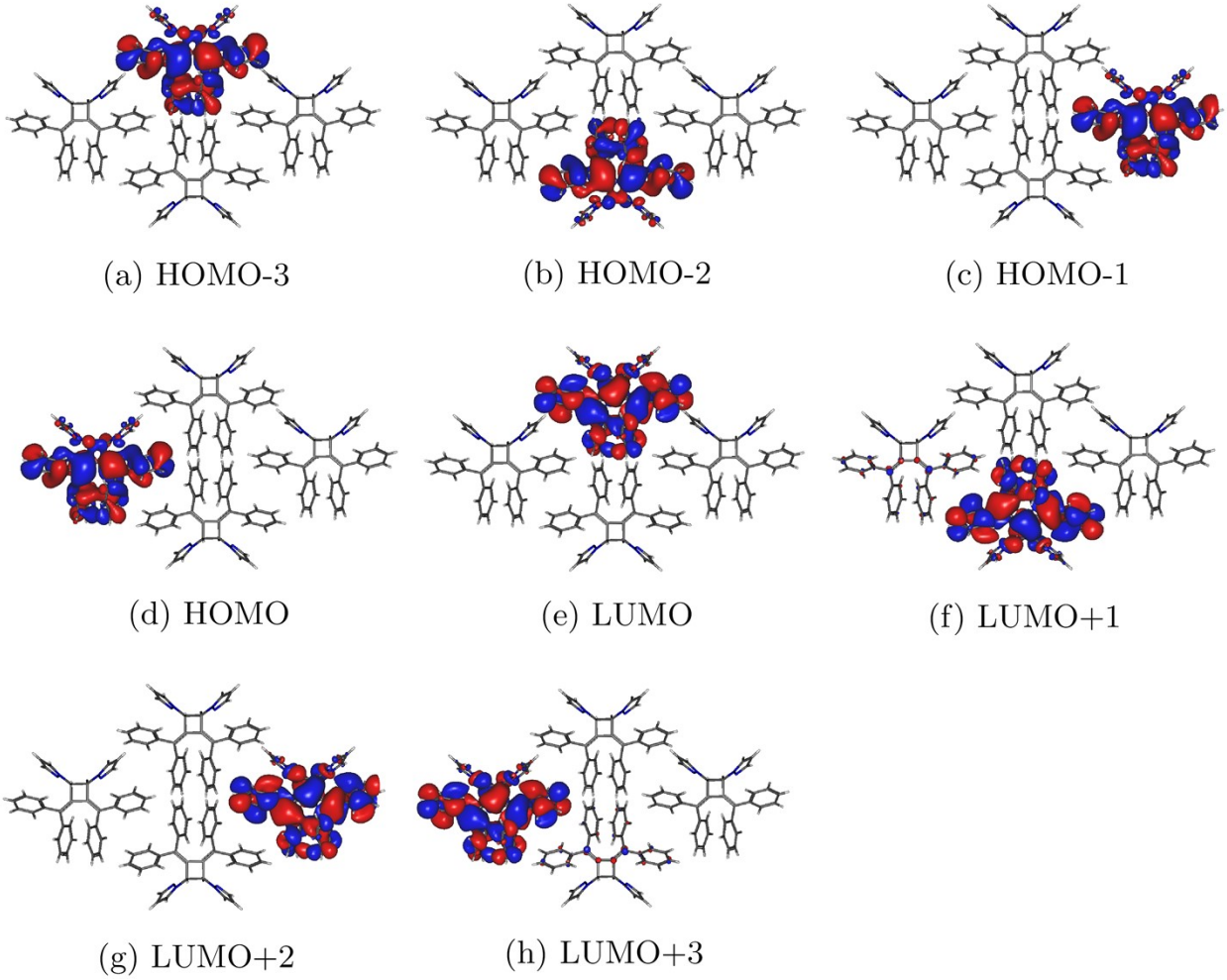

Figure S22: Frontier molecular orbitals from HOMO−3 to LUMO+3 of a representative tetramer selected from the fifteen possible tetramers extracted from the crystal structure.

Table S13: The vertical excitation wavelength (λ, in nm units), oscillator strength (f, dimensionless), electron transition and character of the selected pentamer from the unit cell.

State	λ (nm)	*f*	Electron transition	Character
S_1	387.3	>0.01	HOMO → LUMO	CT
S_2	381.4	>0.01	HOMO-1 → LUMO	LE
S_3	380.8	>0.01	HOMO→ LUMO+3	LE
S_4	379.3	>0.01	HOMO-2 → LUMO	CT
S_5	378.9	>0.01	HOMO-1→ LUMO+4	LE
S_6	378.8	>0.01	HOMO → LUMO+1	CT
S_7	376.1	>0.01	HOMO-2 → LUMO+1	CT
S_8	371.9	>0.01	HOMO-3 → LUMO	CT
S_9	364.5	>0.01	HOMO-2 → LUMO+1	CT
S_{10}	363.6	0.20	HOMO → LUMO+4 HOMO-1 → LUMO+3	LE
S_{11}	358.8	>0.01	HOMO-4 → LUMO HOMO-3 → LUMO+1	LE
S_{12}	358.1	>0.01	HOMO-1 → LUMO+2 HOMO-2 → LUMO+2	CT
S_{13}	356.5	3.45	HOMO-3 → LUMO+1 HOMO-1 → LUMO+3	LE
S_{14}	355.7	>0.01	HOMO-4 → LUMO HOMO-1 → LUMO+2	CT
S_{15}	353.9	0.03	HOMO-2 → LUMO+2	LE

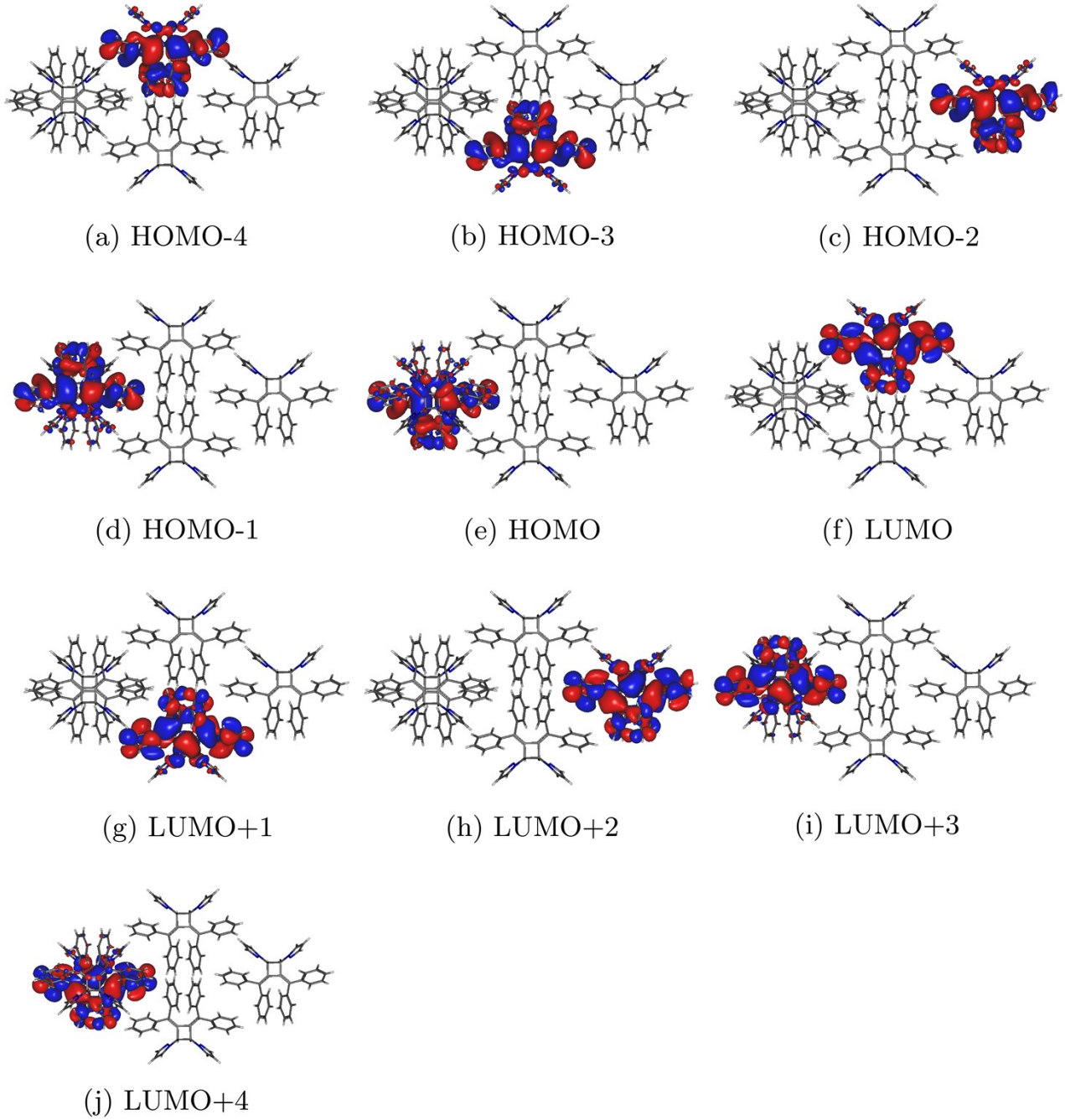

Figure S23: Frontier molecular orbitals from HOMO−4 to LUMO+4 of a representative pentamer selected from the six possible pentamers extracted from the crystal structure.

Table S14: The vertical excitation wavelength (λ, in nm units), oscillator strength (f, dimensionless), electron transition and character of the selected hexamer from the unit cell.

State	λ (nm)	*f*	Electron transition	Character
S_1	385.2	>0.01	HOMO → LUMO HOMO-1 → LUMO+1	
S_2	385.2	>0.01	HOMO → LUMO+1 HOMO-1 → LUMO	
S_3	383.1	>0.01	HOMO → LUMO+1 HOMO-1 → LUMO	
S_4	383.1	>0.01	HOMO → LUMO HOMO-1 → LUMO+1	
S_5	382.3	>0.01	HOMO-2 → LUMO+1 HOMO-3 → LUMO+2	
S_6	382.3	>0.01	HOMO-2 → LUMO+2 HOMO-3 → LUMO+1	
S_7	380.7	>0.01	HOMO-1 → LUMO+1 HOMO → LUMO+2	
S_8	380.7	>0.01	HOMO-1 → LUMO+2 HOMO → LUMO+1	
S_9	378.8	>0.01	HOMO-2 → LUMO+4 HOMO-3→ LUMO+3	
S_{10}	378.8	>0.01	HOMO-2 → LUMO+3 HOMO-3→ LUMO+4	
S_{11}	377.3	>0.01	HOMO-2 → LUMO+1 HOMO-3→ LUMO	
S_{12}	377.3	>0.01	HOMO-2 → LUMO HOMO-3→ LUMO+1	
S_{13}	364.1	0.54	HOMO → LUMO+4 HOMO-1→ LUMO+5 HOMO-2 → LUMO+2 HOMO-3→ LUMO+3	LE
S_{14}	363.3	>0.01	HOMO → LUMO+5 HOMO-1→ LUMO+4 HOMO-2 → LUMO+3 HOMO-3→ LUMO+2	
S_{15}	362.4	>0.01	HOMO-4 → LUMO HOMO-5→ LUMO+1	
S_{16}	362.4	>0.01	HOMO-4 → LUMO+1 HOMO-5→ LUMO	
S_{17}	359.6	>0.01	HOMO-4 → LUMO+1 HOMO-5→ LUMO	
S_{18}	356.9	3.77	HOMO-4 → LUMO HOMO-5→ LUMO+1 HOMO-3 → LUMO+2 HOMO-2→ LUMO+3	LE
S_{19}	352.5	>0.01	HOMO → LUMO+3 HOMO→ LUMO+2 HOMO-1 → LUMO+2 HOMO-1→ LUMO+3	

S_{20}	352.5	>0.01	HOMO → LUMO+3 HOMO→ LUMO+2 HOMO-1 → LUMO+2 HOMO-1→ LUMO+3

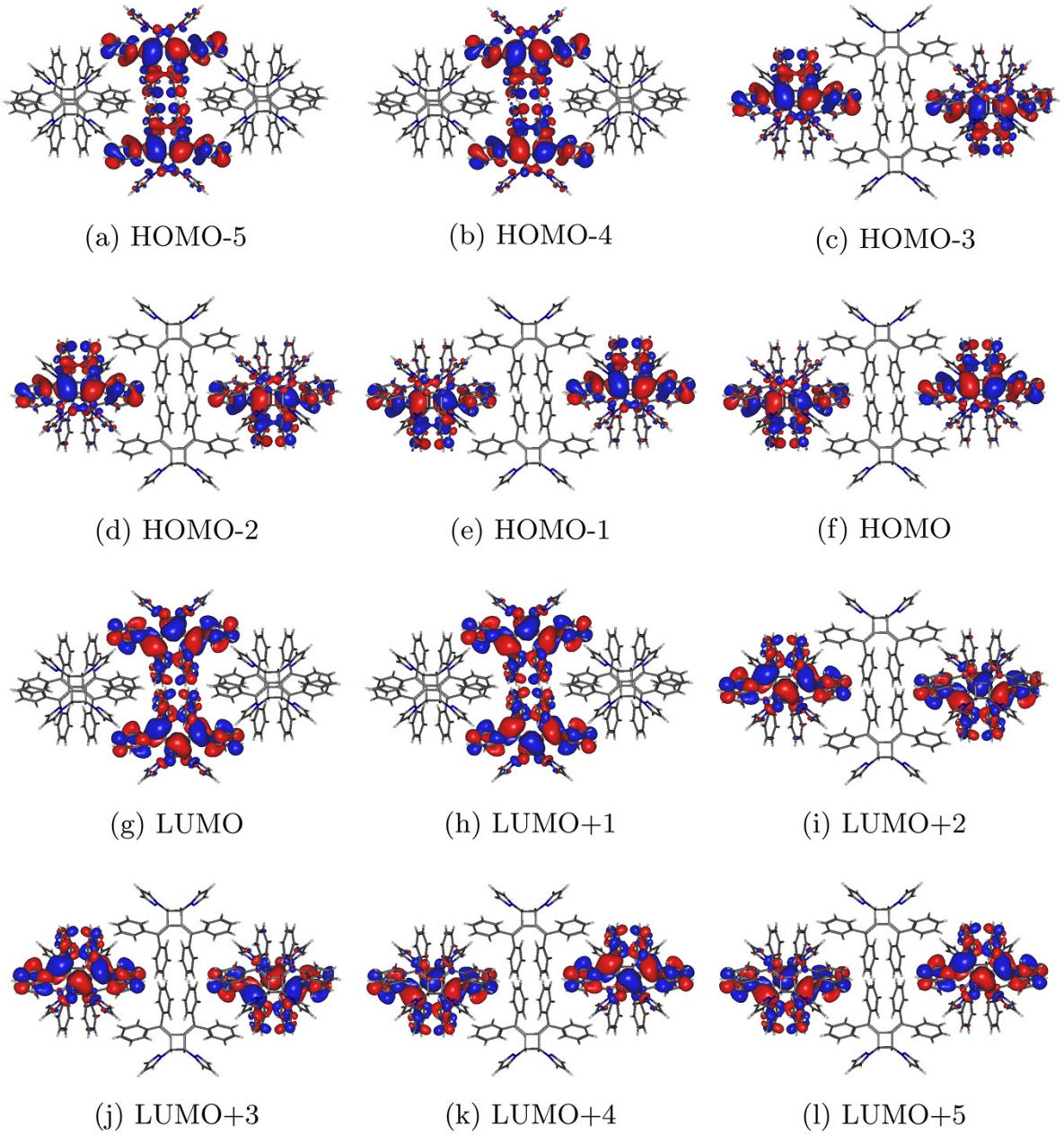

Figure S24: Frontier molecular orbitals from HOMO −5 to LUMO+5 of a representative hexamer extracted from the crystal structure.

Table S15: Excited state energies employing a cluster model (mono, di, tri, tetra, penta and hexamer) from the crystal structure.

	No of geometries studied	Lowest State energy (nm)	Standard Deviation (nm)	Energy of Bright State (nm)	Oscillator strength
Monomer	1	354.4	-	354	0.74
Dimer	15	354.8-379.7	9.01	355	1.54
Trimer	20	364.8-381.2	5.12	358	2.38
Tetramer	11	373.2-383.5	2.76	360	1.52
Pentamer	4	382.2-387.3	2.41	363	0.20
Hexamer	1	385.2	-	364	0.54

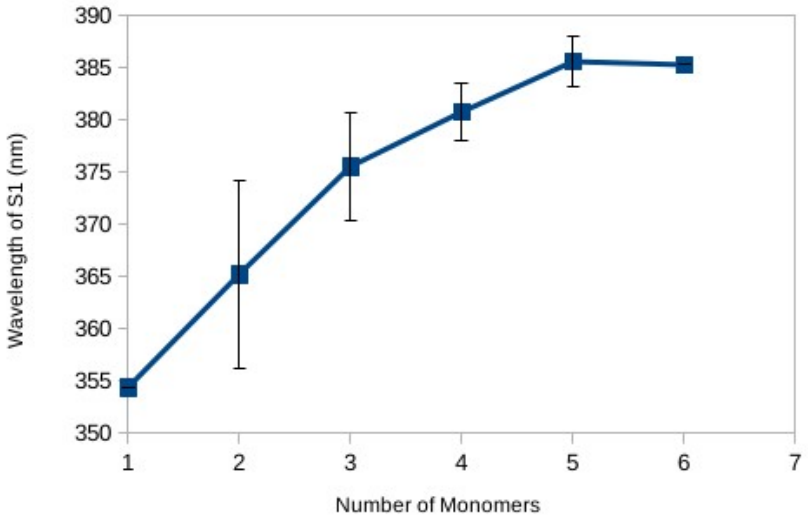

Figure S25: The average excitation energy of the first electronic state (S_1) along with the standard deviation for mono, di, tri, tetra, penta and hexamers obtained from the crystal structure.

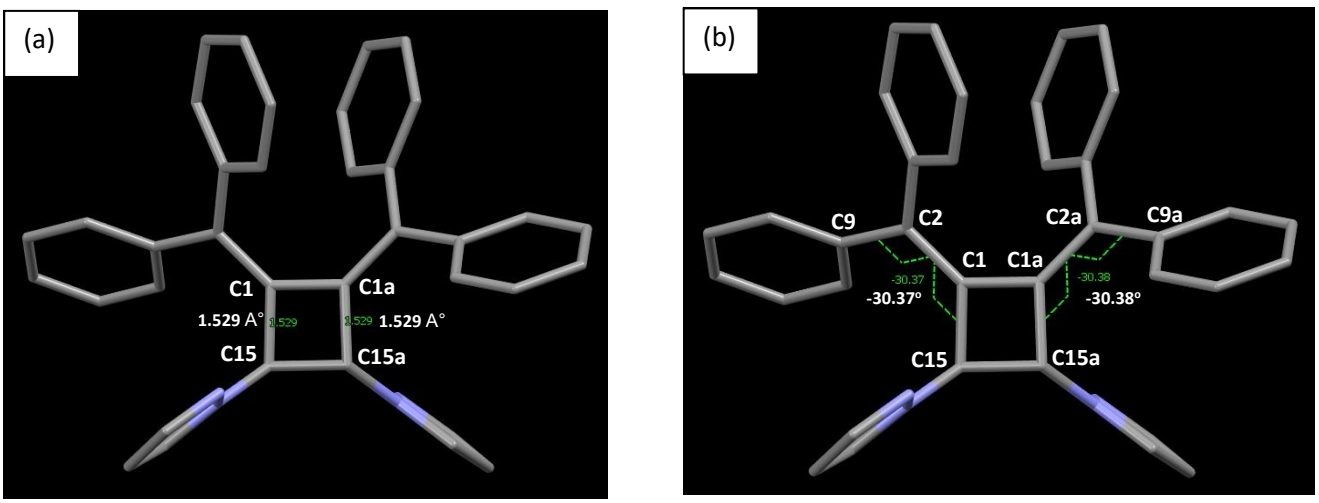

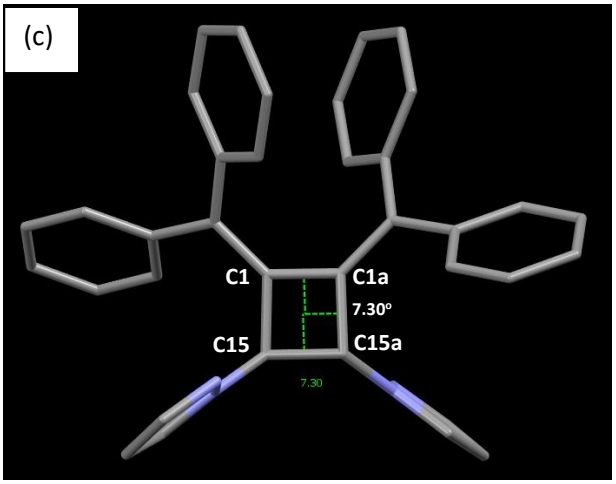

Figure S26: Excited state S1 optimized geometry bond lengths (C1-C15 and C1a-C15a), torsion angles (C15-C1-C2-C9, C15C1a-C2a-C9a) and (C1-C1a-C15a-C15) are shown in the figures (a), (b) and (c) using mercury software from CCDC.

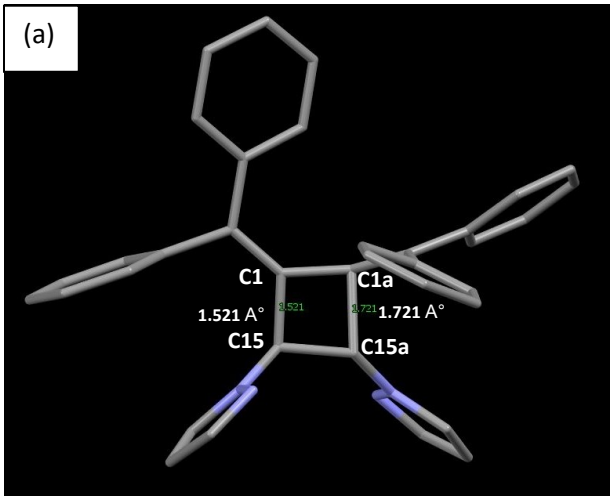

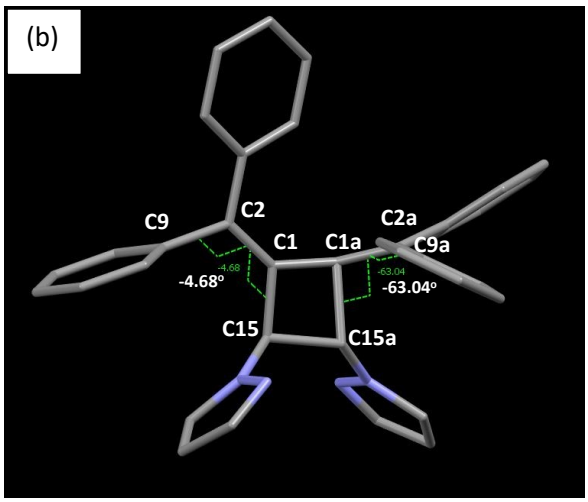

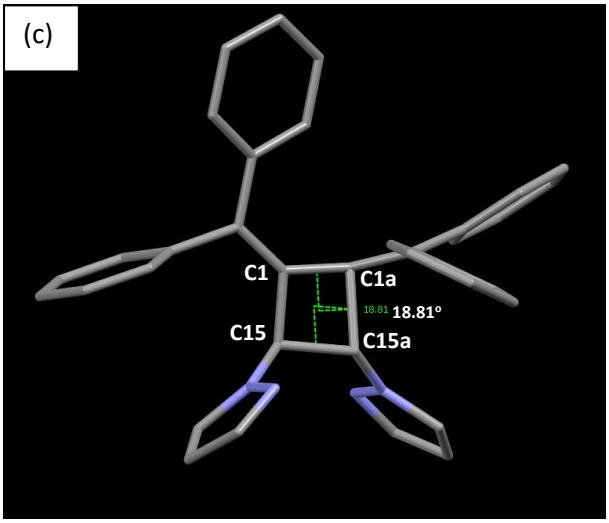

Figure S27: CI state geometry bond lengths bond lengths (C1-C15 and C1a-C15a), torsion angles (C15-C1-C2-C9, C15-C1a-C2a-C9a) and (C1-C1a-C15a-C15) are shown in the figures (a), (b) and (c) using mercury software from CCDC.

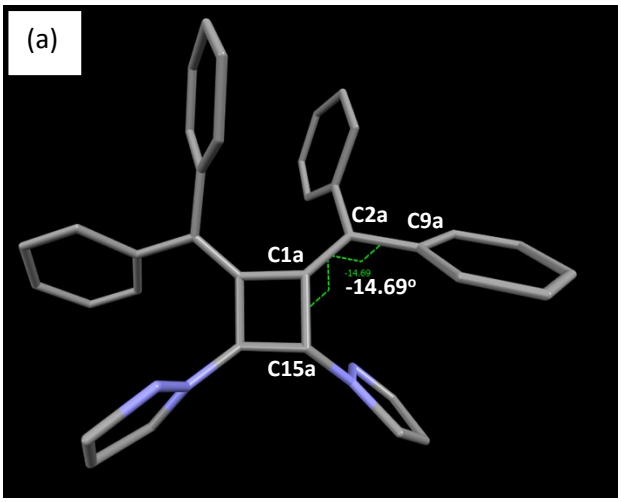

Figure S28: Geometry from the un-optimized crystal structure showing a torsion angles (C15-C1a-C2a-C9a) using mercury software from CCDC.

10. References:

1 M. E. Zandler and F. D'Souza, *Comptes Rendus Chim.*, 2006, **9**, 960–981.
2 M. Orio, D. A. Pantazis and F. Neese, *Photosynth. Res.*, 2009, **102**, 443–453.
3 Z. Chen and J. Yang, *Front. Phys. China*, 2006, **1**, 339–343.
4 J. Wang and B. Durbeej, *J. Comput. Chem.*, 2020, **41**, 1718–1729.
5 D. F. Tegegn, H. Z. Belachew and A. O. Salau, *Sci. Rep.*, 2024, **14**, 8146.
6 R. El Mouhi, S. El Khattabi, M. Hachi, A. Fitri, A. T. Benjelloun, M. Benzakour, M. Mcharfi and M. Bouachrine, *Res. Chem. Intermed.*, 2019, **45**, 1327–1340.
7 A. Jendoubi, Y. Arfaoui, J. Palaudoux, M. M. Al-Mogren and M. Hochlaf, *J. Comput. Chem.*, 2024, **45**, 563–573.
8 S. H. El-Demerdash, S. A. Halim, A. M. El-Nahas and A. B. El-Meligy, *Sci. Rep.*, 2023, **13**, 15626.
9 J. Tirado-Rives and W. L. Jorgensen, *J. Chem. Theory Comput.*, 2008, **4**, 297–306.
10 M. Aydin, *Density Funct. Theory-Recent Adv. New Perspect. Appl.* 2019
11 R. D'Cunha and T. D. Crawford, *J. Phys. Chem. A*, 2021, **125**, 3095–3108.
12 J. Hernández-Lima, K. Ramírez-Gualito, B. Quiroz-García, A. L. Silva-Portillo, E. Carrillo-Nava and F. Cortés-Guzmán, *Front. Chem.*, 2022, **10**, 1012769.
13 D. F. S. Machado, T. O. Lopes, I. T. Lima, D. A. da Silva Filho and H. C. B. de Oliveira, *J. Phys. Chem. C*, 2016, **120**, 17660–17669.
14 A. V Marenich, C. J. Cramer and D. G. Truhlar, *J. Phys. Chem. B*, 2009, **113**, 6378–6396.
15 Y. Takano and K. N. Houk, *J. Chem. Theory Comput.*, 2005, **1**, 70–77.
16 L. Xu, Towards Improving The Accuracy of Implicit Solvent Models and Understanding Electrostatic Catalysis in Complex Solvent Environment. 2022.
17 F. Neese, F. Wennmohs, U. Becker and C. Riplinger, *J. Chem. Phys.*, 2020, **152**, 224108
18 F. Neese, *Faraday Discuss.*, 2024, **254**, 295–314.
19 F. Neese, *Wiley Interdiscip. Rev. Comput. Mol. Sci.*, 2012, **2**, 73–78.
20 R. Guareschi and C. Filippi, *J. Chem. Theory Comput.*, 2013, **9**, 5513–5525.
21 F. Plasser, *J. Chem. Phys*. 2020, **152**, 084108.